Local Measurements of the Spatial Magnetic Field Distribution in a Z-Pinch Plasma During and Near Stagnation Using Polarization Spectroscopy

G. Rosenzweig,[1, a)] E. Kroupp,[1] T. Queller,[1] A. Starobinets,[1] Y. Maron,[1] V. Tangri,[2] J. L. Giuliani,[3] and A. Fruchtman[4]

[1)]*Faculty of Physics, Weizmann Institute of Science, Rehovot 7610001, Israel*
[2)]*Research Support Instruments, Lanham, MD 20706, USA*
[3)]*Plasma Physics Division, Naval Research Laboratory, Washington, DC 20375, USA*
[4)]*Department of Physics, Holon Institute of Technology, Holon 5810201, Israel*

(Dated: 24 January 2020)

We present here the detailed measurements of radial distribution of the magnetic field in a gas-puff z-pinch plasma at the final stages of the implosion phase and at stagnation. While the measurements are chordal, the radial distribution of different charge states was utilized to measure the magnetic field locally for certain radii, so that, unlike chordal measurements in general, the magnetic field radial distribution was obtained with no need for Abel inversion of the data. The distribution was measured using the Zeeman effect via a novel spectroscopic technique, at several axial locations, and demonstrates striking features such as the peak field remaining at a radius much larger than the stagnation radius at all times. Furthermore, while the distribution observed is sometimes monotonic with respect to radius, it is often not, a behavior that can be linked to 2D features in the plasma column resulting from the Rayleigh-Taylor instability. The current flowing through the stagnating plasma was found to be a small fraction of the total current, resulting in clearly insufficient magnetic pressure to balance the plasma pressure at stagnation. The magnetic field data, taken over several axial positions, are used to obtain the true inductance in the imploding plasma for the first time; it is found it cannot explain the current turnover at stagnation. A simulation with the MACH2-TCRE magnetohydrodynamics code in the $r-z$ plane shows that the peak of the magnetic field pinches to a much smaller radius than is observed in the spectroscopic data. Furthermore, the depth of the computed current turnover at stagnation is smaller than the measured one. The two observed features of a radially extended magnetic field at stagnation together with a deep current turnover are a challenge to match in simulations. Various calculations and estimates of the inductive and resistive load voltages are examined to ascertain if they are responsible for the observed current notch. The results demonstrate that knowledge of the true inductance in the driven load requires such magnetic-field-distribution measurements, and that imaging data or electrical measurements are insufficient.

PACS numbers: 32.60.+i, 32.70.Jz, 52.58.Lq, 52.65.-y, 52.70.Ds, 52.70.Kz,

I. INTRODUCTION

One of most the elusive, yet crucially important properties of an imploding plasma is the magnetic field distribution in the various stages of the implosion. Both the characteristics of the stagnation process and the efficiency of the energy coupling to the plasma are strongly dependent on the plasma-field interaction. Therefore, this distribution is heavily relied upon in theoretical models and simulation schemes of z-pinch plasmas for predicting the hydrodynamic and atomic processes[1,2].

Determination of magnetic fields in plasmas using Zeeman-effect-based spectroscopic methods is limited in studying high-energy-density (HED) systems due to their sensitivity to density- or temperature-induced broadenings[3]. Zeeman-split patterns are smeared out by broad spectral line-shapes that result from the high densities and high ion velocities, even when the π-Zeeman components are removed from the spectrum with polarization techniques[4]. Alternative approaches, namely Faraday rotation, $\dot{B}$ probes, or proton beam deflectometry, each suffer from their own difficulties[5]. By way of illustration, Faraday rotation requires knowledge of the electron density values throughout the plasma and the use of Abel inversion, as was done in Ref. 6 for a wire-array z-pinch; $\dot{B}$ probes are intrusive and offer limited resolution; and proton beam deflectometry necessitates high power beam sources and extensive 3D simulations and is truly not practical in z-pinch experiments. The coherent fields, which proton trajectory integrates over long lengths, produce deflections too large to measure. For a 1 MA z-pinch, multi-MeV protons are necessary to measure fields successfully[7]. Thus, using other techniques to measure the field, like the one presented in this paper, are crucial.

Zeeman splitting remains therefore attractive as a non-intrusive tool and has indeed been used to measure magnetic fields in imploding plasma experiments[4,5,8–12]. However, to date the effect was mainly employed to measure the field in z-pinches at a single radial position. Expanding the usefulness of Zeeman-based spectroscopy for HED plasma conditions must include experimentally obtaining the magnetic field spatial distribution, rather than determine the field magnitude in a limited region. To the best of our knowledge, as yet only in Ref. 4 was the Zeeman effect used to measure this distribution in z-pinch investigations. These measurements were limited to relatively far from the stagnating plasma ($r > 7$ mm) and to times earlier than 90 ns before stagnation on axis.

[a)]Electronic mail: guy.rosenzweig@gmail.com; Present address: Plasma Science and Fusion Center, Massachusetts Institute of Technology, Cambridge, MA 02139, USA

In this paper we present magnetic field radial distributions measured before, during and after stagnation of a z-pinch plasma, closer to the pinch axis than ever achieved before. These measurements were made using "the two-polarizations method" described in detail in Ref. 5. This method, previously employed only at the outermost radius of the plasma column in a z-pinch experiment[10], offers the highest sensitivity to the field magnitude of all the Zeeman-based methods. The two-polarizations method utilizes the naturally formed gradients in the plasma properties to obtain $B(r)$, and without the need for an Abel inversion. After discussing the data we present a section on modeling with a radiation-magnetohydrodynamics (MHD) simulation code and examine the load voltage based on the current profile.

II. DIAGNOSTIC METHOD

A. The two-polarizations method

The diagnostic method is thoroughly described in Refs. 5 and 13. In short, when the perturbation in the energy levels due to the magnetic field is small compared to the fine-structure energy separations, the magnetic-field-induced splitting for both the upper and the lower levels of the transition is given by

$$\Delta E = g_{LSJ}\mu_B MB, \tag{1}$$

where B is the magnitude of the magnetic field $\vec{B}$, M is the projection of the total angular momentum J of the given state in the direction of $\vec{B}$, μ_B is the Bohr magneton, and g_{LSJ} is the Landé g factor[14]. If a dominant direction of $\vec{B}$ exists, the emissions from the components of a Zeeman split transition are polarized. When the emission is viewed parallel to $\vec{B}$, only its σ components are visible and the light is circularly polarized, right handed for σ^+ ($\Delta M = +1$) and left handed for σ^- ($\Delta M = -1$).

Discriminating between the σ^+ and σ^- components, observed along multiple chords through the plasma, is achieved by means of a quarter-wave plate and a polarizing beam-splitter. The radiation is split into two beams, each carrying one of the now orthogonal linear polarizations, and directs each beam to a different branch of a bifurcated optical fiber array. The joint end of the array is imaged onto the entrance slit of a 1.26-m spectrometer equipped with a 2400 grooves/mm grating. The spectra of both polarizations are recorded simultaneously by an intensified charge-coupled-device (ICCD) camera coupled to the exit focal plane of the spectrometer.

While the σ^+ components are always blue-shifted with respect to the unpolarized emission line, the σ^- components are always red-shifted. This method therefore relies on the line positions rather than on their shapes, and is thus applicable even when the lines are Stark- and Doppler-dominated and is nearly unaffected by opacity.

B. Use of various charge states to obtain radial dependence using the chordal observations

The diagnostic method can only be used with lines of sight that are parallel to $\vec{B}$. This appears to yield only a single data-point per experiment, which provides B (the magnitude of $\vec{B}$) at the outermost radius of the plasma column. Using Ampère's law (see Eq. (2)) this data-point provides only the total current flowing through the plasma. In contrast, in this work we overcame this limitation and were able to penetrate into the plasma column and directly determine the magnetic field radial distribution. We accomplished this by taking advantage of the naturally occurring charge-state radial distribution and recording spectral lines emitted from different charge states simultaneously.

In both low- and high-current z-pinch experiments producing a high K-shell emission yield, only $\sim 15\%$ of the imploding plasma is heated at stagnation to conditions necessary to radiate K emission[1,15]. This generates a considerable temperature gradient dropping from the hot core towards the peripheral plasma, which in turn generates a radial charge-state distribution, from highly charged ions found at the core, to lower charge states that reside at outer layers (as illustrated in Fig. 1). Therefore, the field radial distribution can be measured by observing the Zeeman effect from emissions of several charge states simultaneously, each emitted from the outermost radius for which a satisfactory signal is obtained.

III. EXPERIMENTAL SETUP

The lumped circuit model of the z-pinch generator is comprised of a capacitor bank (5.5 μF), charged to 60 kV, in series with a resistor (20 mΩ), an inductor (30 nH), and the gas-puff load with initial inductance of 1.1 ± 0.5 nH. The generator drives a peak current of 500 kA, rising in 500 ns as measured by a calibrated $\dot{B}$ probe. The oxygen gas-puff is injected through a double nozzle comprised of a central opening of diameter 2.6 mm and an outer annular opening spanning 34.4 to 38 mm in diameter. The nozzle exit plane is recessed by 4 mm from the edge of an annular sleeve serving as the cathode. The anode wire mesh is also housed in an annular sleeve and is set back 5 mm from the edge of the annulus. There is a 9 mm gap between the cathode edge and the anode edge.

The oxygen gas-puff consists of an on-axis jet, ~ 5 mm in diameter, surrounded by thick shell. Due to radial expansion of the shell along the flow towards the anode, the shell is initially conical with an outer diameter of ~ 40 mm at the nozzle, which extends to nearly 60 mm close to the anode(see Fig. 3(a)). Stagnation on axis is reached in ~ 500 ns and lasts ~ 10 ns, during which x-rays are emitted (dashed red line in Fig. 2).

The spatial, temporal and spectral resolutions of the polarization spectroscopy setup discussed in Section II A are 1 mm, 10 ns and ~ 0.31 Å, respectively. These provided sufficient signal-to-noise ratio (SNR) and a minimum detectable field of 2×10^4 G. An additional spectroscopic system, featuring a mapped optical fiber array, imaging optics, a 30 cm spectrom-

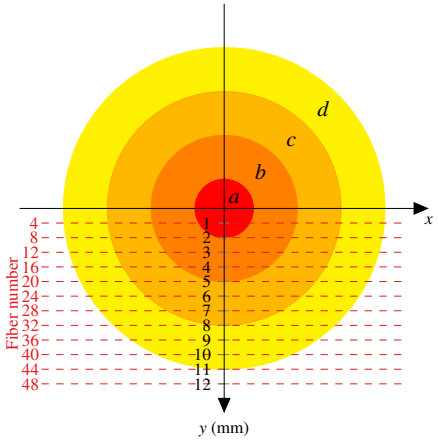

FIG. 1. Schematic top view of a layered plasma column and the chordal views. As an example, four layers are described, each containing different charge states. Twelve lines of sights, out of the 50 provided by the fiber array, are displayed by red dashed lines, with their ordinal numbers in the array given on the left. These lines of sight are parallel to the x-axis and are evenly spaced along the y-axis (chordal positions). Lines of sight closer to $y = 0$ mm collect contributions from more charge states. In this illustration, only the lines of sight tangent to the outer edges of the different layers, namely at $y = 2, 5, 8,$ and 11 mm, can provide reliably the magnetic field magnitude. Adapted from Ref. 5, © Sissa Medialab. Reproduced by permission of IOP Publishing. All rights reserved.

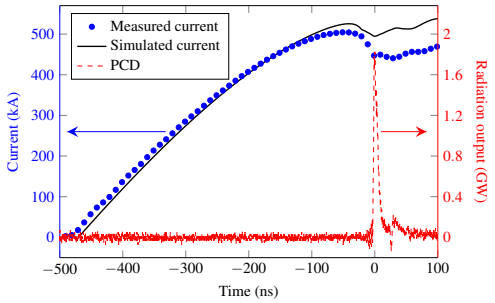

FIG. 2. Measured and simulated current profiles and x-ray emission measured by the PCD for the oxygen gas-puff pinch of shot 2277. The simulated current was obtained from a MACH2-TCRE simulation (see Section VI C).

eter and an additional ICCD camera, was employed simultaneously with the diagnostics described above. This system provided a broad spectral range which was used for obtaining the electron temperatures (T_e) and densities (n_e) from line intensity ratios[16–18], determining the Stark and Doppler broadenings mentioned in the next Section.

A third ICCD camera is operated concurrently with the spectrometer ICCD, to record 2D side-on UV-visible-light images of the plasma (Fig. 3). These images provide a better understanding of the spectrograms obtained, and provide the outermost radius of the plasma column, used to calculate the boundary magnetic field, B_0, as explained below.

IV. DATA ANALYSIS

Figure 2 shows a typical current profile and an x-ray pulse. When the rising part of the current profile is aligned for all the shots discussed below, the implosion time is 500 ± 25 ns. The ~ 10 % variation in implosion time arises from the variation in the mass loading. To compare shots near stagnation with a common fiducial time, we set $t = 0$ in the magnetic field data presented below to mark the time of the x-ray pulse peak.

Figure 3 presents a sequence of 2D UV-visible images, from the second ICCD camera mentioned above, of the gas-puff implosion from eight different shots. The gas nozzle is at the top in each image and $z = 0$ is the edge of the cathode. Polarization spectroscopy for the magnetic field was performed at $z = 2$, 5 and 8 mm. The outer radius of the plasma, $R_0(t)$, is chosen to be the outer edge of the recorded emission. This outer radius is used later to evaluate the magnetic field at the vacuum-plasma boundary.

The two spectral lines used in this work are the O VI 3811.35-Å line and the O III 3791.26-Å line. These lines are in spectral proximity, so that they can be simultaneously observed by the spectrometer with adequate resolution, yet they are isolated from each other and from neighboring lines for the plasma parameters typical of our experiments. The charges of O VI and O III are sufficiently different so that they reside in distinctively different radii. The outermost radius of each charge-state layer was determined by examining the intensities of the spectral lines obtained from the various fibers. Since the diagnostic method does not require Abel inversion, any asymmetry viewed in the UV-visible images has limited effect on the measured magnetic-field values, and only due to the possibility that the line of sight is not parallel to $\vec{B}$. However, an uncertainty in the viewing angle is already taken into consideration, as discussed in the last paragraph of this section.

Since the lines are isolated, their Stark broadening shapes are Lorentzian. Other contributions to the line shapes broadening, namely the Doppler broadening and the instrumental spectral response, are nearly Gaussian. Therefore, inferring the magnetic field magnitude from a measured line requires fitting a Voigt profile to each polarization line shape, from which the wavelength of its peak is obtained.

The spectral separation, $2\Delta\lambda$, between the peaks of the σ^+ and the σ^- profiles of each line is compared with a Zeeman splitting calculation. This calculation takes into account the Stark, Doppler and instrumental broadenings, since the position of the peak of each σ polarization may depend on these broadenings when there is more than one transition with $\Delta M = +1$ and more than one with $\Delta M = -1$. Calculations

for the spectral lines measured in this research proved that the dependence of $\Delta\lambda$ on the broadening mechanisms is almost negligible; incorporating it into the error analysis contributed a little to the error bars.

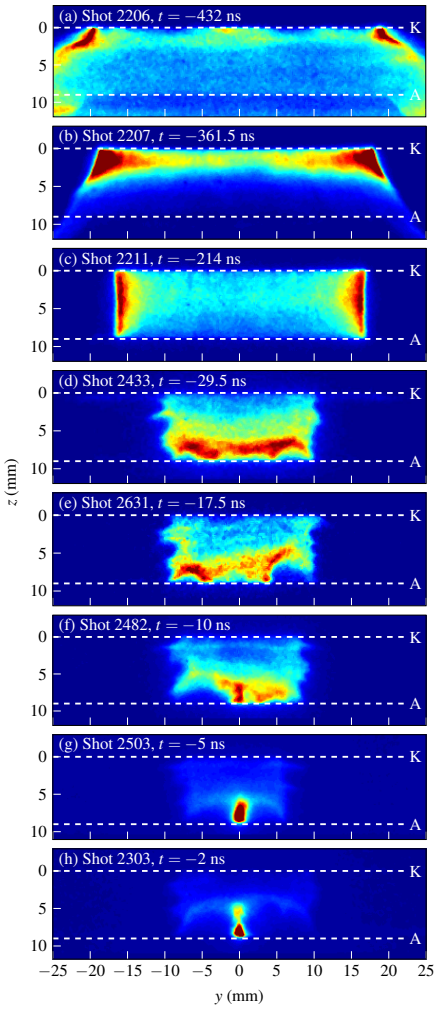

FIG. 3. 2D UV-visible images of the plasma during the implosion of the oxygen gas z-pinch. The magnetic field measurements presented below are obtained from a fiber array viewing normal to the y-direction (see Fig. 1) at $z = 2$, 5 and 8 mm. Each image has been normalized separately for display purposes, and the color coding does not translate between the images. Nozzle and cathode are at the top.

Additional sources of errors result from light being captured by the optical elements from a spread of angles. These are: a slight ellipticity of the polarizations, variation in the retardance of the quarter-wave plate and alteration of the diattenuation (polarizing efficiency) of the polarizing beam splitter. It is noteworthy that all three mechanisms cause the splitting to become *smaller* than it would be in their absence, thus making the derived magnitude of the magnetic field be a lower bound for its true value. The combined uncertainty from all these effects was demonstrated to be smaller than 5% for our system, and was therefore incorporated in the upper error bar. These sources of errors, as well as the dependence on the broadening mechanisms, are discussed in depth in Ref. 5.

V. RESULTS

Eight magnetic field radial distributions, measured at eight moments in time at $z = 5$ mm, are presented in Fig. 4. We note again that each distribution was obtained from a separate discharge. The field value at the innermost radial position is obtained from the Zeeman splitting of the O VI line. At the next radial position, the value is obtained from the O III line. The error bars for these data-points were derived from the accuracy in which the emission wavelengths could be determined. In some cases the SNR was such that a range of Voigt profiles could be fit, thus increasing the uncertainty. To this, the contribution of the systematic error discussed above were incorporated.

The outermost value, marked with a square, is positioned at the outer radius of the plasma cylinder, R_0 (measured using the 2D plasma images), and is calculated using Eq. (2). The error bars here are a result of the precision by which R_0 could be determined, and the standard deviation of the current within the 10 ns measurement window.

At $t = 1$ ns (Shot 2277, Fig. 4(h)), the outermost radial position of the O III ions is 8 mm. R_0 at the same discharge was measured from the corresponding 2D plasma image to be 8.25 mm. Given the spatial resolution of the diagnostic system, these position are experimentally identical. Indeed, the magnetic field in these two positions is 10.9×10^4 G. The field value at $r = 8$ mm was measured using the Zeeman splitting of the O III line. The field value at R_0 is the boundary magnetic field, B_0, and is obtained via Ampère's law (cgs units), namely

$$B_0 = \frac{2I_0}{R_0 c}, \tag{2}$$

where I_0 is the entire circuit current measured by the $\dot{B}$ probe outside the pinch region, and c is the speed of light.

The agreement between the two methods of calculating B at the plasma edge in this shot, proves that similarly to the results presented in Ref. 4, the entire circuit current flows within the outer radius of the plasma cylinder. Therefore, B_0 is calculated for each discharge and added to each distribution.

Magnetic field distributions at two additional z-positions are given in Figs. 5 and 6. For each z-position, eight moments in time are presented. The distributions at $z = 2$ mm are monotonic: rising from the innermost radius to R_0. However,

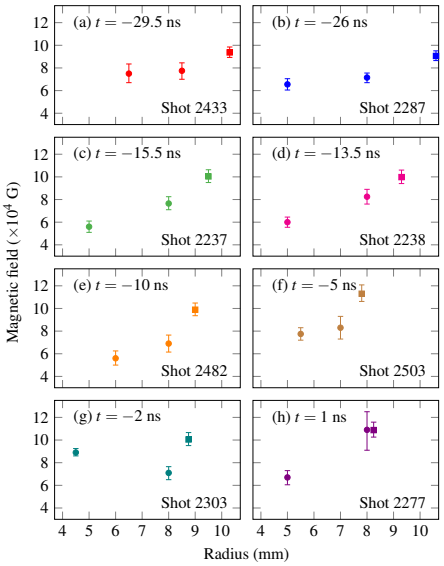

FIG. 4. Magnetic field distributions at eight moments in time and $z = 5$ mm. The circles represent values obtained from the O VI (innermost radii) and the O III spectral lines, and the squares represent the boundary magnetic field, B_0, obtained from I_0. The distribution at $t = 1$ ns (Shot 2277) shows that when the radial position of O III line is almost R_0, the measured magnitude agrees with the value of B_0. This proves that indeed the entire circuit current flows within R_0 and validates the use of Eq. (2) for obtaining B_0.

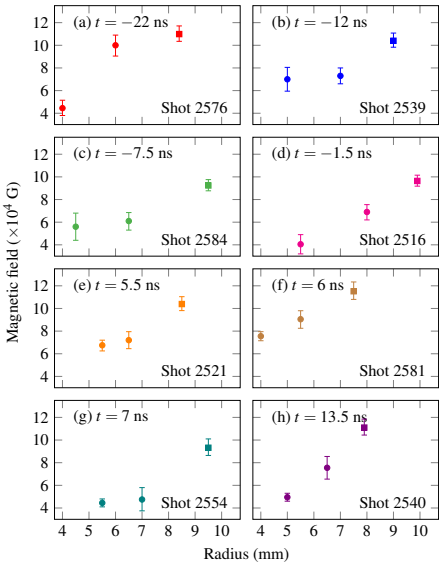

FIG. 5. Magnetic field distributions at eight moments in time and $z = 2$ mm.

those at $z = 8$ mm exhibit a non-monotonic behavior, where B at the innermost radius is larger than at the intermediate radius. These behaviors are dominant at these z-positions when numerous experiments are examined: while very few distributions at $z = 8$ mm show monotonicity, most do not, and none of the distributions at $z = 2$ mm show non-monotonicity. The distributions shown in Fig. 4 demonstrate that at $z = 5$ mm, some distributions are monotonic, while others are not.

VI. DISCUSSION

A. Non-monotonic distributions

While most of the distributions given in Figs. 4-6 show that the magnetic field is monotonically increasing with radius, Fig. 4(g) and most of Fig. 6 (except for Panels (b) and (d)) demonstrate non-monotonic distributions. Such distributions were not seen in the simulation (Fig. 8), which at all times produced a magnetic field that rises from $r = 0$ to the vacuum-plasma boundary, R_0, and then drops as $1/r$ according to Eq. (2).

The image sequence given in Fig. 3 demonstrates how an onset of the Rayleigh-Taylor instability, seen initially in Panel (d), grows as the implosion progresses. At the final stages of the implosion the instability grows to form flaring arcs that curve towards the anode and can be seen in Panels (e)–(h). A similar behavior, even more pronounced, was recorded for neon gas-puff implosions in the same generator[19,20].

Faraday's law

$$\frac{\partial \vec{B}}{\partial t} = -c\nabla \times \vec{E}, \tag{3}$$

can be combined with an Ohm's law for the axial electric field in the plasma

$$E_z = -\frac{\upsilon}{c}B_\theta + \eta J_z = -\frac{\upsilon}{c}B_\theta + \frac{\eta c}{4\pi}\frac{1}{r}\frac{\partial}{\partial r}(rB_\theta), \tag{4}$$

to obtain the induction equation in cylindrical coordinates

$$\frac{\partial B_\theta}{\partial t} = -\frac{\partial}{\partial r}(B_\theta \upsilon_r) - \frac{\partial}{\partial r}\left(\frac{\eta c^2}{4\pi}\frac{1}{r}\frac{\partial}{\partial r}(rB_\theta)\right), \tag{5}$$

where η is the plasma resistivity and υ is the radial velocity.

The first term on the right-hand-side (RHS) is the "advective" term, and the second is the "diffusive" term. The degree to which each of these terms affect the plasma dynamics is quantified by the Lundquist number[21,22]

$$S = \frac{\tau_R}{\tau_A} = \frac{4\pi R_0^2}{\eta c^2}\frac{B}{R_0\sqrt{4\pi\rho}}, \tag{6}$$

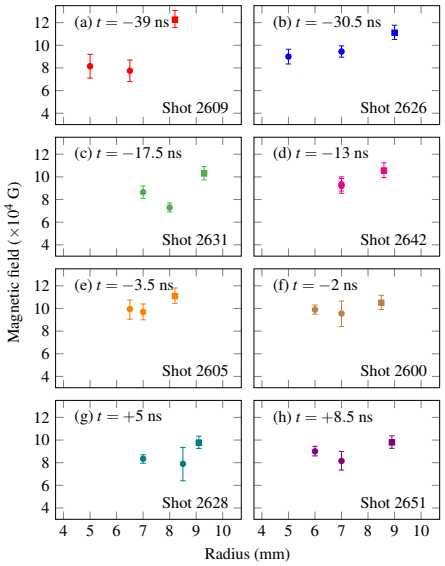

FIG. 6. Magnetic field distributions at eight moments in time and $z = 8$ mm. In (d) the O III and O VI data points overlap. This results from the fact that both charge states were found in the flaring arcs discussed in the text. While the two states cannot coexist and still emit detectable lines[13], for very thin flares they may be too close to be discriminated by the spatial resolution of the diagnostic system. The fact that the independent analysis of both lines yielded the same field magnitude, strengthens the validity of the method and the analysis.

where τ_R is the resistive-diffusion time and τ_A is the Alfvén transit time. $\rho = n_e m_i/\bar{Z}$ is the mass density with $\bar{Z}$ being the mean ion charge and m_i the ion mass. For $S > 1$, advection must be taken into account. During the times of the measurements near the plasma periphery $T_e \simeq 7$ eV, $n_e \simeq 1.5 \times 10^{18}$ cm^{-3}, $B = B_\theta \simeq 10^5$ G, and $\bar{Z} \simeq 2$. With $R_0 \simeq 8$ mm and $\eta = \eta_{Spitzer} \approx 2.8 \times 10^{-15}$ s (Section VI C), these values yield $S \simeq 25$, thus the plasma is advection dominated.

The Lundquist number is a special case of the Magnetic Reynolds number and therefore also represents the extent to which the magnetic field is "frozen in" the plasma. For $S \gg 1$ the magnetic field is frozen into the plasma, and for $S \ll 1$ it freely permeates the conducting plasma. It was recently shown that certain plasma radial velocity profiles can result in unexpected radial magnetic distributions[23]. Here, however, for $S \simeq 25$ the axial plasma flow that accompanies the flaring arcs' formation carries the partially frozen-in magnetic field and distorts the 2D contours of its $r - z$ distribution. This distortion can result in a non-monotonic radial distribution when viewed within the narrow Δz window provided by the diagnostic system, if the flaring arc crosses the measured z-position.

Indeed, inspection of the 2D images associated with non-monotonic distributions shows a correlation between those distributions and the flaring arcs. Shot 2303 at $z = 5$ mm in Figs. 3(h) and 4(g), and shot 2631 at $z = 8$ mm in Figs. 3(e) and 6(c), are examples of this correlation. The flaring arcs *almost always* reach $z = 8$ mm during the times measured in this research, *sometimes* reach $z = 5$ mm and *never* reach $z = 2$ mm, in agreement with the abundance of the non-monotonic distributions. A non-monotonic distribution for the magnetic field at a particular z-position is always associated with a flaring arc at the same z-position.

B. Current distribution

For every measured field magnitude, the entire current flowing within its radial position can be calculated using Eq. (2). Such calculations are presented in Fig. 7 for field distributions displayed in Fig. 4. It is important to note that each data-point represents the current integrated from $r = 0$ to its radius, and not the local current flowing at that radius. It can clearly be seen that only about a third of the total current, I_0, flows within the innermost radius. This result supports the inference in Ref. 24 that less than a quarter of the circuit current flows through the stagnating plasma during stagnation.

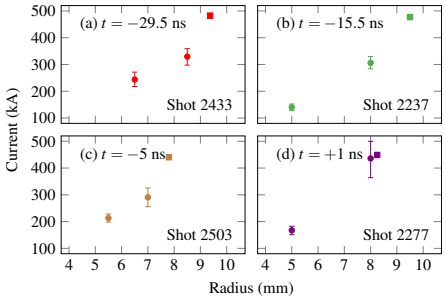

FIG. 7. Integrated current distributions calculated from magnetic field distributions displayed in Fig. 4. The circles represent values calculated from the magnetic field magnitudes using Eq. (2), and the squares represent I_0.

C. Modeling

A striking feature of the data from Figs. 4, 5, and 6 is that the peak of the magnetic field remains at a radius much larger than the stagnation radius of the bright emission seen in Panels (g) and (h) of Fig. 3, while at the same time the current in Fig. 2 displays a strong turnover, or inductive notch, at stagnation. This turnover is observed in all of the shots and is very reproducible, if the peak of the currents are aligned in time and normalized. In a typical z-pinch with a narrow x-ray

emitting region the turnover is attributed to a large change in inductance during the implosion.

In this section we examine the issue of the magnetic field radial distribution by a comparison with simulation and analysis of circuit data. To self-consistently model the nonlinear evolution of the current, the notch as well as the 2D evolution of the magnetic field, we employ the magneto-hydrodynamics code MACH2-TCRE. In general, the code self-consistently evolves plasma density with three components of the velocity and magnetic field in two spatial dimensions in addition to separate equations for the ion and electron temperatures. Here we limit the simulation to 2D cylindrical geometry with velocities in the $r-z$ plane and only consider the azimuthal component of the magnetic field. The circuit solver in MACH2-TCRE is coupled to the MHD through the inductive and the resistive load voltages. In our simulation, we use the classical Spitzer resistivity with the coefficients for the transverse component given by Braginskii coefficients[25]. The resistivity is not a constant but varies in space and time with the electron temperature, as well as charge state and density (through the Coulomb logarithm). This treatment allows for non-linear resistive diffusion of the magnetic field[26] and is more general than the frozen-in approximation of Eq.(6). To account for the non-local-thermodynamic-equilibrium (non-LTE) kinetics, opacity, and non-local transport of radiation, the Tabular Collisional-Radiative Equilibrium (TCRE)[27] was employed for oxygen.

MACH2-TCRE verification tests include the magnetized Noh problem[28] and radiation transport of line emission using long characteristics[29]. Recent validation tests of the multi-physics radiation magnetohydrodynamics with TCRE include argon gas-puff implosions on the Z machine at Sandia National Laboratories[30,31].

MHD simulations of a gas-puff z-pinch require the initial density and the circuit parameters of the driving generator. For the initial density profile, Mach-Zehnder interferometry measurements[32] were interpolated onto the finer MACH2 $r-z$ grid. The circuit parameters were listed in Section III. For the geometry described in Section III, an A-K gap of 9 mm is taken and the return current radius $R_w = 37$ mm. In order to overcome challenges of modeling magnetic field diffusion at high Alfvén speed beyond the vacuum-plasma interface MACH2 uses a hard density floor. A number of simulations varying this floor parameter were performed. From an ensemble of these simulations, the simulation closest to experimental data is presented.

The temporal evolution of the current from this simulation is shown in Fig. 2 as a solid line. The rate of change of current during the run-in phase (when the load inductance is low) matches the solid line in the experiment, but the inductive notch in the experimental current profile is stronger than in the simulation. The x-ray emission, measured by the PCD and shown as a dashed red line in Fig. 2, peaks at 1.7 GW. This is in good agreement with the peak value of 1.4 GW predicted by the simulation.

In Fig. 8, radial distributions of the magnetic field from the MACH2-TCRE simulation are displayed as solid lines during the implosion at five different times. These lines are axially averaged values of the calculated magnetic field over the range $z = 4.5$ to $z = 5.5$ mm and can be compared with the observed values for the magnetic field from Fig. 4 using the same color-time association, due to the experimental spatial resolution of 1 mm. The magnetic field at $t = -29.5$ ns, represented by a solid red line, peaks around $r \approx 8$ mm and the profile at $t = -10$ ns, represented by a solid orange line, peaks around $r \sim 5$ mm. Thus an inward propagating peak in the magnetic field with significant speed can clearly be discerned in the simulation data.

However, the corresponding diagnostic data presented earlier in Fig. 4 and repeated in Fig. 8 does not show an indication of a similarly propagating magnetic peak. Therefore, a much stronger compression of the magnetic field is observed in the simulation results than in the observed data. On the other hand, the simulation finds a smaller current notch than found in the measured current profile of Fig. 2. In the simulations we find that the load voltage is primarily inductive, but this is inconsistent with the observations that the magnetic field is not pinched with the plasma while the current displays a large inductive notch.

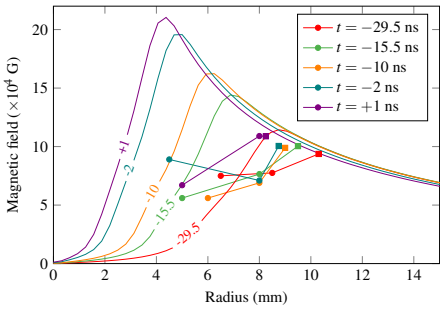

FIG. 8. Radial distribution of the magnetic field at $z = 5$ mm obtained from a MACH2-TCRE simulation (smooth curves) is compared with the diagnostic data (markers connected by straight lines) at $t = -29.5$ ns (red), $t = -15.5$ ns (green), $t = -10$ ns (orange), $t = -2$ ns (teal) and $t = +1$ ns (violet). The color coding matches that of Fig. 4.

The fact that the peak of the magnetic field does not move inward during the implosion, as is seen in the simulations, suggest that there is additional physics in the pinch that is not properly treated in the MHD simulation using MACH2-TCRE. Such physical processes or assumptions that might be responsible for the behavior of the magnetic field include: current losses or arcs in the final feed to the load past the current diagnostic; kinetic treatment of low density plasma; continuous addition of freshly ionized gas beyond the 10 mm radius, that becomes conductive and sweeps in with a low value of the trapped magnetic field; or details of the electrode, nozzle, and return current configuration for this experiment not included in the present simulation. Further research on this issue is not within the scope of this primarily experimental paper. Here what we can readily do is examine what the observed current

notch implies about the load voltage. We can calculate the load voltage from both the current data and separately from the magnetic field measurements. First consider the expression for the load voltage based on the lumped circuit model described in the beginning of Section III:

$$V_{load}^{(I)} = V_0 - \frac{1}{C_g}\int_0^t I dt - L_g\frac{dI}{dt} - \mathcal{R}_g I \tag{7}$$

The temporal evolution of $V_{load}^{(I)}$ can be computed from the measured time history of the current, $I(t)$ for shot 2277 shown in Fig. 2 and the fixed lumped circuit parameters stated at the beginning of Section III. The superscript (I) on the load voltage means that it is calculated from the measured current profile. The result for $V_{load}^{(I)}$ from Eq. (7) is shown in Fig. 9(a) as the blue line. As the capacitor discharges, I increases, the capacitor voltage $V_C = V_0 - 1/C_g\int_0^t I dt$ decreases (dashed orange line), and the energy stored in the capacitor bank is available for the load. Note that this load voltage from the lumped circuit becomes much larger than the voltage from the generator at the time of stagnation, which causes the sharp turnover of the current at this time. The load voltage from the MACH2-TCRE simulation, V_{load}^{sim}, is also shown in the figure. While it is likewise much larger than the capacitor voltage, its maximum is less than $V_{load}^{(I)}$, consistent with the smaller inductive notch in Fig. 2. We do find that the inductive component of V_{load}^{sim} is much larger than the resistive one. The effective load impedance can be calculated from Eq. (7) using $\mathcal{Z}_{load} = V_{load}^{(I)}/I$, and is shown in Fig. 9(b). The peak value of this impedance occurs at $V_{load}^{(I)} \sim 215$ kV and $I \sim 463$ kA, giving $\sim 0.46\ \Omega$.

Next we calculate the load voltage from the magnetic field measurements, $V_{load}^{(B)}$. To formulate the model, integrate Faraday's law, Eq. (3), over a rectangular area in the $r-z$ plane stretching from the z-axis out to the fixed return current radius, R_w, and bounded by the surfaces of the two electrodes in the axial direction (see Fig.III-1 in Ref. 2). Applying Stokes' theorem to the RHS results in two contributions: one for the electric field across the gap in the power feed, and a second from the electric field along $r = 0$. The electrodes and return current rods are considered perfect conductors so the electric field vanishes. Then we have

$$\int_0^{R_w}\frac{1}{c}\frac{\partial}{\partial t}B_\theta dr dz = -\int_{gap} E_r dr - \int_{r=0} E_z dz \tag{8}$$

The first term on the RHS is the load voltage ($E_r < 0$), which we identify with the load voltage from the magnetic field measurement, $V_{load}^{(B)}$. The second term from Eq. (4) is just $\int(\eta J_z)_{r=0}dz$, because the velocity vanishes on the axis. Since the limits of integration on the left hand side are fixed, one can extract the time derivative to obtain

$$V_{load}^{(B)} = \frac{d}{dt}\left(\int\frac{2I}{c^2}\ln\left(\frac{R_w}{R_0(t)}\right)dz + \int_0^{R_0(t)} B_\theta dr dz\right) + (\eta J_z \ell)_{r=0}, \tag{9}$$

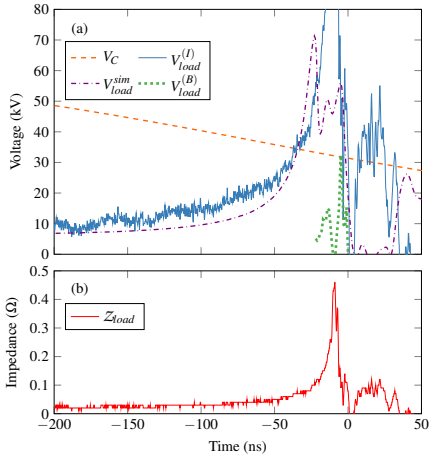

FIG. 9. (a) Load voltages computed from the measured current (blue line), from the simulation (dash-dotted violet line), and from the magnetic field measurements (dotted green line). The discharging capacitor voltage is the dashed orange line. (b) Estimated load impedance. Details of the calculation procedures are explained in the text.

where we have taken the resistive voltage term to be uniform along z at $r = 0$. In this equation we have split out the magnetic flux from Eq. (8) into the vacuum and plasma components, where $R_0(t)$ is the plasma-vacuum interface and can write the inductance from the magnetic field measurements as

$$L_{load}^{(B)} = \frac{2}{c^2}\ln\left(\frac{R_w}{R_0(t)}\right)dz + \frac{1}{I_{load}^{(B)}}\int_0^{R_0(t)} B_\theta dr dz \tag{10}$$

We can now use the data in Figs. 4, 5, and 6 to calculate the inductance $L_{load}^{(B)}$. These figures are for $z = 5$, 2, and 8 mm, respectively, and we weigh them equally so that dz in Eq. (10) equals 3 mm. For the vacuum component the value of $R_0(t)$ is the outermost measured point in these figures and the current $I_{load}^{(B)}$ is based on Eq. (2). For the plasma component, for each panel in these figures we assume the magnetic field varies linearly from $r = 0$ to the innermost position, and likewise linearly between the remaining data points. Now the two magnetic flux terms in Eq. (10) can be evaluated at each of the eight times in the three figures. Since the times of the data are not the same in these figures we have used linear interpolation to map the values onto a common temporal grid. We added to this inductance the vacuum inductance using the measured current from shot 2277 and the average of the plasma-vacuum radius at the proper times. We find that over the time span common to the data in Figs. 4, 5, and 6, namely -22 to $+1$ ns, the value of $L_{load}^{(B)}$ varies only from 2.34 to 2.40 nH and the current from 475 to 446 kA.

With this small variation the time derivative to form the $V_{load}^{(B)}$ in Eq. (9) is quite noisy and shows a maximum of only about 8 kV. The result is shown in Fig. 9 as the dotted green line covering the range from -22 to $+1$ ns. As would be expected by reviewing the data in Figs. 4, 5 and 6, there is little change in the magnetic flux throughout this time interval and the inductive load voltage computed from the magnetic field measurements is negligible compared to the load voltage from the measured current.

The data do not rule out the possibility that there is a region inside of the innermost data position where the magnetic field increases to a maximum and then decreases to zero on the axis. This would be the behavior if there was a strong current density on the axis, which is not necessarily ruled out by the results of Fig. 7 because the current density would be negative beyond the position of the maximum in order to reproduce the measured magnetic field at the innermost position. However to attain the peak load voltage $V_{load}^{(I)} \sim 215$ kV the field would need to increase at a rate of $\sim 2\times10^{14}$ G/s, which seems extreme.

The above calculation for $V_{load}^{(B)}$ ignored any potential contribution from the resistive voltage term in Eq. (9). For the resistivity η, first the Spitzer transverse resistivity evaluated using Braginskii coefficients[25]. For the O III measured point, which is near R_0: $T_e \simeq 7$ eV, $n_e \simeq 1.5\times10^{18}$ cm^{-3}, $B_\theta \simeq 10^5$ G, and $\bar{Z} \simeq 2$. Then $\eta_{Spitzer} \approx 2.8\times10^{-15}$ s $= 2.5\times10^{-3}$ $\Omega\cdot$cm. If the current density on axis is the same as the average value, then the resistive load voltage would be only $(\eta_{Spitzer}\ell/\pi R_0^2)I \approx 230$ V, for $R_0 = 8$ mm and $I = 450$ kA. On the axis the temperature is larger, which would reduce the resistivity, but the current density could be larger. If the temperature on axis is 100 eV and 1/3 of the total current flows on the axis, based on Fig. 7, then classical resistivity could account for $V_{load}^{(I)}$ if the current channel has a radius of ~ 55 μm. The MACH2-TCRE calculations, which include classical resistivity, give no indication of a narrow current channel on axis, at least within the MHD assumptions.

There could be an anomalous resistivity within the pinch that produces a sufficiently large voltage to cause the notch. One such model for a strong anomalous resistivity is the compression of magnetic bubbles developed by Velikovich et al.[33] to explain enhanced energy deposition in z-pinch radiation sources. In this model the magnetic bubbles are buoyantly driven inward during the compression phase of the pinch and dissipate their trapped magnetic energy on the z-axis at stagnation. The effective non-linear resistance in this model is described by

$$\mathcal{R}_{magbub} = \frac{I\ell}{2\mu_m^{1/2}c^3R_0} = \frac{I(\mathrm{MA})\ell(\mathrm{cm})}{2[\mu_m(\mu\mathrm{g/cm})]^{1/2}R_0(\mathrm{mm})} \approx 3.3\times10^{-3}\ \Omega \quad (11)$$

where the evaluation occurs at the stagnation conditions: $I = 450$ kA and $R_0 \sim 8$ mm. This is a hundred times smaller than the maximum experimental impedance of ~ 0.46 Ω shown in Fig. 9(b). There is also the ion-viscous heating model of Haines[34]. The effective resistance of this model is a factor of 4 larger than the formula of Eq. (11), and could not be responsible for current turnover either.

Finally, it is possible that a gap opens up somewhere along the z-axis. In order for Child-Langmuir current to flow across a gap of length d and radial extent s while matching the observed impedance of ~ 0.46 Ω at a gap voltage of, at most, 215 kV, one finds[35] $0.46(s/d)^2 \sim 293$, i.e., the gap radius must be about 25 times the gap length. If some of the voltage drops along the plasma column and the gap voltage is smaller than 215 kV, this ratio becomes even larger. Such a gap geometry is possible, but cannot be confirmed with the present diagnostics.

VII. CONCLUSIONS

The magnetic field distribution was measured at the end of the implosion phase and throughout the stagnation phase of a z-pinch plasma, and was found to be inconsistent with a diffusive pattern. The measurements were made close to the axis of stagnation and at several z-positions. This feat was accomplished by developing and implementing a novel technique based on Zeeman polarization spectroscopy. The individual shapes of the left- and right-circularly polarized components of Zeeman-split emission lines have been recorded simultaneously, thereby overcoming the Stark and Doppler broadenings typical to high-energy-density systems. Selected lines from the O III and O VI charge states, which reside only at distinct radii due to the radial temperature gradient, were exploited to yield the radial distribution of the magnetic field with no need for Abel inversion in spite of the chordal view of the measurements. In addition, measurements of the fundamental properties of the plasma and its structure were made and used for inferring the magnetic field values from the Zeeman-split spectra.

The distribution of the field as a function of radius is rather complex. Several measured distributions cannot be explained easily by a 1D solution of the magnetic diffusion equation[13]. The plasma was found to be advection-dominated, and axial plasma motion, caused by the onset of the Rayleigh-Taylor instability, creates flaring arcs and appears to carry with it the frozen-in magnetic field and distort its structure. This distortion is manifested in unexpected, non-monotonic features in the radial distribution of the field when measured over a small segment of the z-axis. The non-monotonic distributions were not seen in the present simulations and are associated with the existence of flaring arcs at the same z-positions in which they were measured.

It was found that the current flowing through the stagnating plasma is a rather small fraction of the total current. The magnetic pressure close to the axis proves to be insufficient to balance the stagnation-plasma pressure, strengthening a previous result based on energy-balance calculations, which showed this balance is provided by the imploding-plasma dynamic pressure[24].

The MACH2-TCRE MHD code was employed to simulate the pinch. The simulation shows (i) that there is a turnover

in the current at stagnation due to the inductive voltage, and (ii) that the peak of the magnetic field moves inward with the plasma to a small radius ($\sim$ 3 mm) during the stagnation phase. However, the simulated turnover, or notch, is not as large as found in the experimental current profile, and the measured magnetic field distribution shows the peak of the magnetic field remains at about 8 to 10 mm during stagnation. These observed features appear to be inconsistent with each other if the current notch arises from an inductive load voltage. Additional physics such as plasma kinetics, current losses, or a more exact modeling of the load geometry may be responsible for these differences. We next examined what the load voltage must be to account for the notch based on the measured current and compared that with the load voltage from the MACH2-TCRE simulation and as calculated from the magnetic field measurements. Both the simulated and calculated load voltage from the magnetic field are smaller than that determined by the current data. A sharp rise in the current density within the innermost measured position for the magnetic field to produce a large inductive voltage cannot be ruled out, though no such feature is observed in the MACH2-TCRE simulations. We next examined whether a resistive voltage could be responsible for the current notch. Estimates using classical or anomalous resistivity do not appear to fit the requirements, but a gap with Child-Langmuir flow is a possible explanation.

One caveat to the analysis discussed immediately above is that the temporal resolution of the magnetic field measurements is similar to the stagnation time of 10 ns. It is possible that the data in Figs. 4, 5 and 6 have not captured the implosion dynamics. The positions of the signals from the O III and O VI emission lines are taken to be the outermost radius where the emission is observed. If the plasma compresses to a much smaller radius during the gate time, our approach would attribute a larger radius to the pinch. One solution to resolve this uncertainty would be to perform Zeeman polarization spectroscopy on emission lines from a higher charge state than O VI, that only appears in the hottest region of the pinch. This effort could also address the question of whether there is a large current density and magnetic field interior to the present innermost measured position.

It was shown that to truly determine the inductance in the driven load, magnetic-field-distribution measurements, such as were made here, are necessary. Inductance estimations based on imaging data or electrical measurements are insufficient.

The innovative spectroscopic technique is seen to provide rather new experimental information on the magnetic field distribution, and thus new insights into the dynamics of the imploding and stagnating plasma are presently being sought for. This technique can be expanded to serve as a highly valuable diagnostic tool for various high-energy-density plasma systems. When suitable emission lines cannot be found to yield the field distribution in a given system, several doping schemes can be used to seed the medium with suitable tracers. Thus, the technique will hopefully provide previously unattainable information in other experiments too.

ACKNOWLEDGMENTS

We thank A. Fisher and H. S. Staruss for invaluable suggestions and fruitful discussions, and P. Meiri for his skillful assistance. This research is supported by the Israel Science Foundation (grant No. 692/13), the Cornell Multi-University Center of Excellence for Pulsed-Power-Driven High-Energy-Density Science (USA), and at NRL by the US Department of Energy/National Nuclear Security Administration under Grant DE-NA0001564.

[1] D. D. Ryutov, M. S. Derzon, and M. K. Matzen, "The physics of fast Z pinches," Rev. Mod. Phys. **72**, 167–223 (2000).
[2] J. L. Giuliani and R. J. Commisso, "A Review of the Gas-Puff *Z*-Pinch as an X-Ray and Neutron Source," IEEE Trans. Plasma Sci. **43**, 2385–2453 (2015).
[3] R. Doron, D. Mikitchuk, C. Stollberg, G. Rosenzweig, E. Stambulchik, E. Kroupp, Y. Maron, and D. A. Hammer, "Determination of magnetic fields based on the Zeeman effect in regimes inaccessible by Zeeman-splitting spectroscopy," High Energy Density Phys. **10**, 56–60 (2014).
[4] G. Davara, L. Gregorian, E. Kroupp, and Y. Maron, "Spectroscopic determination of the magnetic-field distribution in an imploding plasma," Phys. Plasmas **5**, 1068–1075 (1998).
[5] G. Rosenzweig, E. Kroupp, A. Fisher, and Y. Maron, "Measurements of the spatial magnetic field distribution in a z-pinch plasma throughout the stagnation process," J. Instrum. **12**, P09004–P09004 (2017).
[6] G. S. Sarkisov, B. Etlicher, V. V. Yan'kov, S. Attelan, C. Rouille, and A. S. Shikanov, "Structure of the magnetic fields in Z-pinches," J. Exp. Theor. Phys.+ **81**, 743–752 (1995).
[7] V. Munzar, D. Klir, J. Cikhardt, B. Cikhardtova, J. Kravarik, P. Kubes, and K. Rezac, "Investigation of Magnetic Fields in Z-Pinches via Multi-MeV Proton Deflectometry," IEEE Trans. Plasma Sci. **46**, 3891–3900 (2018).
[8] F. C. Jahoda, F. L. Ribe, and G. A. Sawyer, "Zeeman-Effect Magnetic Field Measurement of a High-Temperature Plasma," Phys. Rev. **131**, 24–29 (1963).
[9] N. J. Peacock and B. A. Norton, "Measurement of megagauss magnetic fields in a plasma focus device," Phys. Rev. A **11**, 2142–2146 (1975).
[10] R. P. Golingo, U. Shumlak, and D. J. D. Hartog, "Note: Zeeman splitting measurements in a high-temperature plasma," Rev. Sci. Instrum. **81**, 126104 (2010).
[11] M. R. Gomez, S. B. Hansen, K. J. Peterson, D. E. Bliss, A. L. Carlson, D. C. Lamppa, D. G. Schroen, and G. A. Rochau, "Magnetic field measurements via visible spectroscopy on the Z machine," Rev. Sci. Instrum. **85**, 11E609 (2014).
[12] J. T. Banasek, J. T. Engelbrecht, S. A. Pikuz, T. A. Shelkovenko, and D. A. Hammer, "Measuring 20-100 T B-fields using Zeeman splitting of sodium emission lines on a 500 kA pulsed power machine," Rev. Sci. Instrum. **87**, 11D407 (2016).
[13] G. Rosenzweig, *Investigation of the magnetic field distribution and the fundamental properties of an imploding plasma, near and during stagnation*, Ph.D. thesis, Feinberg Graduate School, WIS (2015).
[14] E. Stambulchik, K. Tsigutkin, and Y. Maron, "Spectroscopic Method for Measuring Plasma Magnetic Fields Having Arbitrary Distribution of Direction and Amplitude," Phys. Rev. Lett. **98**, 225001 (2007).
[15] E. Kroupp, D. Osin, A. Starobinets, V. Fisher, V. Bernshtam, L. Weingarten, Y. Maron, I. Uschmann, E. Förster, A. Fisher, M. E. Cuneo, C. Deeney, and J. L. Giuliani, "Ion Temperature and Hydrodynamic-Energy Measurements in a *Z*-Pinch Plasma at Stagnation," Phys. Rev. Lett. **107**, 105001 (2011).
[16] L. Gregorian, V. Bernshtam, E. Kroupp, G. Davara, and Y. Maron, "Use of emission-line intensities for a self-consistent determination of the particle densities in a transient plasma," Phys. Rev. E **67**, 016404 (2003).
[17] L. Gregorian, E. Kroupp, G. Davara, V. I. Fisher, A. Starobinets, V. A. Bernshtam, A. Fisher, and Y. Maron, "Electron density and ionization dynamics in an imploding z-pinch plasma," Phys. Plasmas **12**, 092704 (2005).
[18] L. Gregorian, E. Kroupp, G. Davara, A. Starobinets, V. I. Fisher, V. A. Bernshtam, Y. V. Ralchenko, and Y. Maron, "Electron-temperature and energy-flow history in an imploding plasma," Phys. Rev. E **71**, 056402 (2005).
[19] D. Osin, E. Kroupp, A. Starobinets, G. Rosenzweig, D. Alumot, Y. Maron,

A. Fisher, E. Yu, J. L. Giuliani, and C. Deeney, "Evolution of MHD Instabilities in Plasma Imploding Under Magnetic Field," IEEE Trans. Plasma Sci. **39**, 2392–2393 (2011).
[20]J. L. Giuliani, J. W. Thornhill, E. Kroupp, D. Osin, Y. Maron, A. Dasgupta, J. P. Apruzese, A. L. Velikovich, Y. K. Chong, A. Starobinets, V. Fisher, Y. Zarnitsky, V. Bernshtam, A. Fisher, T. A. Mehlhorn, and C. Deeney, "Effective versus ion thermal temperatures in the Weizmann Ne z-pinch: Modeling and stagnation physics," Phys. Plasmas **21**, 031209 (2014).
[21]T. J. M. Boyd and J. J. Sanderson, *The Physics of Plasmas* (Cambridge University Press, 2003).
[22]J. D. Huba, *NRL PLASMA FORMULARY Supported by The Office of Naval Research* (Naval Research Laboratory, Washington, DC, 2018).
[23]I. E. Ochs, C. Stollberg, E. Kroupp, Y. Maron, A. Fruchtman, E. J. Kolmes, M. E. Mlodik, and N. Fisch, "Current channel evolution in ideal Z pinch for general velocity profiles," Submitted to Phys. Plasmas.
[24]Y. Maron, A. Starobinets, V. I. Fisher, E. Kroupp, D. Osin, A. Fisher, C. Deeney, C. A. Coverdale, P. D. Lepell, E. P. Yu, C. Jennings, M. E. Cuneo, M. C. Herrmann, J. L. Porter, T. A. Mehlhorn, and J. P. Apruzese, "Pressure and energy balance of stagnating plasmas in z-pinch experiments: Implications to current flow at stagnation," Phys. Rev. Lett. **111**, 035001 (2013).
[25]S. I. Braginskii, "Transport Processes in a Plasma," Rev. Plasma Phys. **1**, 205 (1965).
[26]P.-A. Gourdain, M. B. Adams, J. R. Davies, and C. E. Seyler, "Axial magnetic field injection in magnetized liner inertial fusion," Phys. Plasmas **24**, 102712 (2017).
[27]J. W. Thornhill, J. L. Giuliani, Y. K. Chong, A. Dasgupta, and J. P. Apruzese, "Improved non-local radiation coupling for MACH2-TCRE," in *2012 Abstracts IEEE International Conference on Plasma Science* (2012) pp. 2C–3–2C–3.
[28]A. L. Velikovich, J. L. Giuliani, S. T. Zalesak, J. W. Thornhill, and T. A. Gardiner, "Exact self-similar solutions for the magnetized Noh Z pinch problem," Phys. Plasmas **19**, 012707 (2012), https://doi.org/10.1063/1.3678213.
[29]J. Apruzese and J. Giuliani, "Multi-dimensional radiation transport for modeling axisymmetric Z pinches: Ray tracing compared to Monte Carlo solutions for a two-level atom," J. Quant. Spectrosc. Ra. **111**, 134 – 143 (2010).
[30]J. Thornhill, J. Giuliani, Y. Chong, A. Velikovich, A. Dasgupta, J. Apruzese, B. Jones, D. Ampleford, C. Coverdale, C. Jennings, E. Waisman, D. Lamppa, J. McKenney, M. Cuneo, M. Krishnan, P. Coleman, R. Madden, and K. Elliott, "Two-dimensional radiation MHD modeling assessment of designs for argon gas puff distributions for future experiments on the refurbished Z machine," High Energ. Dens. Phys. **8**, 197–208 (2012).
[31]V. Tangri, A. J. Harvey-Thompson, J. L. Giuliani, J. W. Thornhill, A. L. Velikovich, J. P. Apruzese, N. D. Ouart, A. Dasgupta, B. Jones, and C. A. Jennings, "Simulations of Ar gas-puff Z-pinch radiation sources with double shells and central jets on the Z generator," Phys. Plasmas **23**, 101201 (2016).
[32]G. Rosenzweig, *Determining the density distribution of a gas injected through a multi-nozzle system for plasma implosion experiments*, Master's thesis, Feinberg Graduate School, WIS (2007).
[33]A. L. Velikovich, J. Davis, J. W. Thornhill, J. L. Giuliani, L. I. Rudakov, and C. Deeney, "Model of enhanced energy deposition in a Z-pinch plasma," Phys. Plasmas **7**, 3265–3277 (2000).
[34]M. G. Haines, "Viscous Heating At Stagnation In Z-Pinches," (2009) pp. 57–60.
[35]Y. Raizer, V. Kisin, and J. Allen, *Gas Discharge Physics* (Springer Berlin Heidelberg, 1997).